Volume 8
Number 44
28 November 2020
Pages 15473–15870

Journal of Materials Chemistry C

Materials for optical, magnetic and electronic devices

rsc.li/materials-c

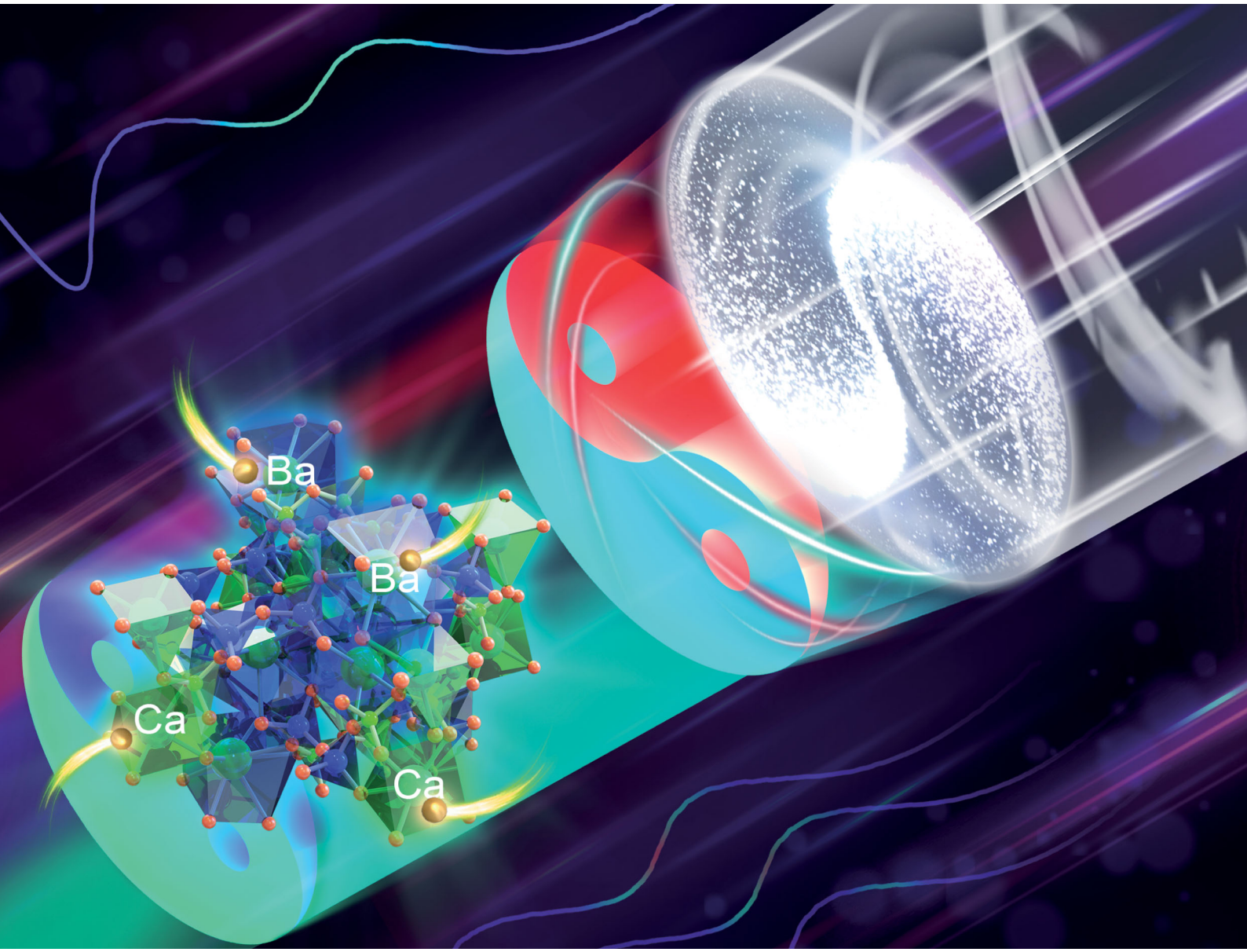

ISSN 2050-7526

ROYAL SOCIETY OF CHEMISTRY

PAPER

Jakoah Brgoch, Rong-Jun Xie *et al.*

Dual-site occupancy induced broadband cyan emission in $Ba_2CaB_2Si_4O_{14}:Ce^{3+}$

Journal of Materials Chemistry C

ROYAL SOCIETY OF CHEMISTRY

PAPER

View Article Online
View Journal | View Issue

Cite this: J. Mater. Chem. C, 2020, 8, 15626

Dual-site occupancy induced broadband cyan emission in $Ba_2CaB_2Si_4O_{14}:Ce^{3+}$†

Shihai You, ‡[ab] Ya Zhuo, ‡[b] Qiulin Chen,[a] Jakoah Brgoch *[b] and Rong-Jun Xie *[a]

Received 2nd June 2020,
Accepted 21st July 2020

DOI: 10.1039/d0tc02625e

rsc.li/materials-c

There is a significant need to identify cyan-emitting phosphors capable of filling the "cyan-gap" (480–520 nm) in full-visible-spectrum phosphor-converted white light-emitting diodes (pc-wLEDs). Here, a new broadband cyan-emitting phosphor that enables addressing of this challenge is reported. The compound, $Ba_2CaB_2Si_4O_{14}:Ce^{3+}$, presents a bright cyan emission peaking at 478 nm with a large full width at half maximum of 142 nm (6053 cm^{-1}), and minimal thermal quenching. The photoluminescence properties originate from Ce^{3+} residing at two different crystallographic sites, a [BaO_9] distorted elongated square pyramid and a [CaO_6] trigonal prism. This combination results in an efficient, broad emission covering the blue to green region of the visible spectrum. Fabricating a simple dichromatic ultraviolet (λ_{ex} = 370 nm) pumped pc-wLED using $Ba_2CaB_2Si_4O_{14}:Ce^{3+}$ along with a commercially available red phosphor demonstrates full-visible-spectrum white light with high color rendering index (R_a > 90) and tunable correlated color temperature, showing the potential of this material for achieving high-quality LED-based lighting.

1. Introduction

Phosphor-converted white light-emitting diodes (pc-wLEDs) have permeated our daily life as lighting sources due to their significant energy savings.[1–4] Currently, a majority of commercially produced pc-wLEDs are based on the simple dichromatic approach, where a single yellow-emitting $Y_3Al_5O_{12}:Ce^{3+}$ (YAG:Ce^{3+}) phosphor is excited by a blue LED chip (λ_{em} = 440–470 nm). This produces high luminous efficacy; however, the lack of a red spectral component in this design causes the artificial light to suffer from a low color rendering index (CRI, R_a < 75) and a high correlated color temperature (CCT > 4500 K).[5,6] Moreover, the sharp, unconverted blue light emitted from the LED chip has been suggested to have hazardous effects on our health, including negatively impacting our circadian rhythm.[7–9] An alternative approach for producing white light is to combine an ultraviolet (UV), or near-UV LED with trichromatic (blue/green/red) phosphors. This approach has been shown to overcome nearly all the drawbacks mentioned above.[10–12] The ratio of blue-/green-/red-emitting materials can be finely adjusted to create white light with a high R_a (~90) as well as tunable CCTs. More importantly, the blue component of the emission spectrum in this design is relatively broad and is weaker in intensity, reducing the negative effects caused by the bright blue LED emission. There are still challenges, however, in generating high-quality full-visible-spectrum white light using this approach. The currently available blue- and green-emitting phosphors in such a device are not able to fully cover the cyan region (480–520 nm) of the visible spectrum, resulting in a "cyan gap".[13–15] Although this gap in UV-driven pc-wLEDs is not as significant as in the blue LED-based lighting devices, its presence still severely inhibits the production of human-centric, full-visible-spectrum white lighting that mimics sunlight. Hence, discovering cyan-emitting phosphors capable of closing this gap in UV-driven LEDs is also of great importance.

This motivation has resulted in great efforts to identify cyan-emitting phosphors using various inorganic hosts, such as silicates,[13,16–19] aluminates,[20–22] nitrides,[15,23–25] sulfides,[26] phosphates,[14,27] vanadates,[28] and borates.[29–31] However, compared to a large number of developed red-, green-, blue- and yellow-emitting phosphors, the quantity of cyan-emitting phosphors remains small. Moreover, many of the reported cyan-emitting phosphors fail to meet the basic criteria for general lighting applications. Most of these materials have either low quantum efficiency, large thermal quenching, or poor chemical stability.[4] Nevertheless, there has been some moderate success. Recently, a borate cyan-emitting phosphor (λ_{em} = 480 nm), $NaMgBO_3:Ce^{3+}$, was shown to possess a high internal quantum efficiency (IQE) of 93% and excellent thermal stability (96% emission intensity retention at 420 K). Its emission band covers

[a] College of Materials, Xiamen University, Xiamen, Fujian 361005, China. E-mail: rjxie@xmu.edu.cn
[b] Department of Chemistry, University of Houston, Houston, Texas 77204, USA. E-mail: jbrgoch@uh.edu

† Electronic supplementary information (ESI) available. See DOI: 10.1039/d0tc02625e

‡ These authors contributed equally to this work.

the blue and cyan regions of the visible spectrum and can successfully achieve full-visible-spectrum white light as a substitute for the blue component, like $BaMgAl_{10}O_{17}:Eu^{2+}$, in the trichromatic pc-wLEDs.[31] Similarly, $Na_{0.5}K_{0.5}Li_3SiO_4:Eu^{2+}$ shows a bright cyan-emission (λ_{em} = 486 nm) with high efficiency and good thermal robustness. This compound produces an extremely narrow emission with a full width at half maximum (fwhm) of 20.7 nm (864 cm^{-1}) that allows it to be added in addition to the blue-, green-, and red-emitting phosphors to produce the tetrachromatic full-visible-spectrum white light.[13]

The trichromatic (cyan/green/red) or tetrachromatic (blue/cyan/green/red) approach enables uniform, full-visible-spectrum white light. However, using multiple phosphors in a single pc-wLED device will always increase the cost, complexity to manufacture, and cause other problems, for example the reabsorption induced efficiency loss.[16] Moreover, the different thermal quenching behaviors of each phosphor will also lead to small but noticeable changes in the generated white light (*i.e.*, chromaticity coordinates and CCTs) during operation. One of the solutions to these problems is to reduce the number of phosphors used in a single device. For example, a broadband cyan-emitting phosphor, $Ba_9Lu_2Si_6O_{24}:Ce^{3+}$, with a fwhm of 118 nm (4519 cm^{-1}), can substitute for both blue- and green-emitting phosphors. By combining this silicate phosphor and a red-emitting $CaAlSiN_3:Eu^{2+}$ with a 395 nm UV LED chip, one can create efficient and high-quality white light (R_a = 90.6 and CCT = 4913 K).[16] This result shows that developing cyan-emitting phosphors with a broad emission band covering the blue, cyan and green regions of the visible spectrum could be a solution to some of the problems caused by using complicated phosphor mixtures.

One approach considered by the phosphor community for producing a broadband emission is to accommodate the activator ions at different crystallographic sites. The combination of different emissions of activators with varying crystal field splitting environments will broaden the total emission. Indeed, a series of broadband phosphors has been developed using this idea.[32–38] For example, an orange-emitting $Y_3Si_5N_9O:Ce^{3+}$ phosphor with a fwhm of 178 nm (4413 cm^{-1}) was produced by substituting Ce^{3+} for two Y^{3+} ions with very different local environments.[32] Recently, a novel yellow-emitting phosphor $Li_2CaSi_2N_4:Ce^{3+}$ with a large fwhm of 165 nm (5329 cm^{-1}) was developed.[34] This broadband emission originates from two distinct Ce^{3+} luminescent centers in the host. Similarly, broadbands $Y_3Si_6N_{11}:Ce^{3+}$ (fwhm = 150 nm; 4423 cm^{-1}) and $La_2MgZrO_6:Cr^{3+}$ with a double-perovskite structure (fwhm = 210 nm; 3045 cm^{-1}) have also been reported.[37,38] These investigations suggest that forming multiple luminescent centers would effectively yield broadband emissions in various phosphor systems.

Inspired by the idea of multi-site engineering, we identified a broadband cyan-emitting borosilicate phosphor, $Ba_2CaB_2Si_4O_{14}:Ce^{3+}$ (BCBSO:Ce^{3+}). The optical properties of this phosphor make it a great candidate for high-quality, full-visible-spectrum pc-wLEDs. BCBSO is a mineral that was first discovered in 2014.[39] Here, we report a laboratory-synthesized version for the first time. The crystal structure has two distinct crystallographic sites, a 9-fold coordinated Ba^{2+} site and a 6-fold coordinated Ca^{2+} site. Both these sites are options for rare-earth ion occupancy to produce a phosphor. In this work, we target the simultaneous occupancy of both sites with Ce^{3+} to generate a broadband cyan emission. The dual-site occupancy is studied in detail using structure and photoluminescence analysis. BCBSO:Ce^{3+} has a relatively high quantum efficiency (54%), excellent thermal stability (95% emission intensity retention at 420 K), and a large fwhm (142 nm; 6053 cm^{-1}). The suitability of this phosphor to cover the blue, cyan, and green regions was further probed by constructing a pc-wLED. Combining BCBSO:Ce^{3+} with a single red-emitting $Sr_2Si_5N_8:Eu^{2+}$ phosphor (dichromatic approach) successfully generates high-quality, full-visible-spectrum cool white light (R_a = 91, CCT = 7052 K) under 370 nm LED excitation. Moreover, the CCT can be widely tuned by mixing an additional green-emitting β-SiAlON:Eu^{2+} phosphor (trichromatic approach), creating a warm white light with outstanding light quality (R_a = 95, CCT = 3651 K). These results demonstrate that BCBSO:Ce^{3+} is a promising cyan component in creating simple but high-quality, full-visible-spectrum white light.

2. Experimental section

2.1 Synthesis

$(Ba_2Ca)_{1-2x/3}Ce_xLi_xB_2Si_4O_{14}$ (BCBSO:xCe^{3+}, x = 0, 0.005, 0.01, 0.015, 0.02, 0.03, 0.05) samples were synthesized *via* the conventional solid-state reaction using $BaCO_3$ (Johnson Matthey, 99.99%), $CaCO_3$ (Alfa Aesar, 99%), H_3BO_3 (Sigma-Aldrich, 99.95%), SiO_2 (Sigma-Aldrich, 99.5%), Li_2CO_3 (Alfa Aesar, 99.998%) and CeO_2 (Sigma-Aldrich, 99.995%). The starting materials were weighed out in the desired stoichiometric ratios and thoroughly ground using an agate mortar and pestle for ~30 min. The homogenous mixtures were then transferred into alumina crucibles and heated at 600 °C for 4 h in air to decompose the reagents. These powders were then reground and heated at 910 °C for 24 h under a reducing atmosphere (5% H_2/95% N_2). After sintering, the products were finely ground for subsequent characterizations.

2.2 Characterization

The phase purity of all samples was first confirmed using a Panalytical X'Pert Pro powder X-ray diffractometer equipped with Cu Kα radiation (λ = 1.54183 Å). The high-resolution synchrotron powder X-ray diffractograms were collected at 295 K with a calibrated wavelength of λ = 0.457893 Å using beamline 11-BM at the Advanced Photon Source, Argonne National Laboratory.[40] Rietveld refinements were conducted using the EXPGUI interface and GSAS software.[41,42] The final crystal structure was visualized using VESTA.[43] Scanning electron microscopy (SEM) images and elemental mappings were obtained using a field-emission scanning microscope (Quanta 650, FEI) equipped with an energy dispersive X-ray spectroscope (EDS, Hitachi S5500). The photoluminescence measurements were performed by encapsulating the phosphor powder in silicone resin (RTV 615, GE Silicones) and depositing the mixture onto a

quartz slide (Chemglass). Steady-state photoluminescence spectra at room temperature were recorded on a PTI QuantaMaster fluorescence spectrophotometer with a 75 W xenon arc lamp as the excitation source. Temperature-dependent emission spectra were collected using a Janis liquid nitrogen cryostat (VPF-100) to control the temperature ranging from 300 to 580 K. The photoluminescence internal quantum efficiency (IQE) was measured by placing the silicone resin encapsulated sample in an integrating sphere (150 mm in diameter, Labsphere) with an excitation wavelength of 350 nm and calculated by applying the method of de Mello *et al.*[44,45] The luminescence lifetime was determined using a Horiba DeltaFlex Lifetime System with a N-330 nano-LED excitation source (λ_{ex} = 336 nm). The fabrication of a pc-wLED involved using the as-prepared BCBSO:0.03Ce^{3+} cyan-emitting phosphor and a laboratory-made $Sr_2Si_5N_8$:Eu^{2+} red-emitting phosphor. A mixture of these two phosphors was encapsulated in silicone resin and then coated on a UV LED (λ_{ex} = 370 nm, Thorlabs). To further tune the CCT of pc-wLEDs, an additional β-SiAlON:Eu^{2+} green-emitting phosphor (Mitsubishi Chemical Corporation) was also used. The electroluminescence spectra, CRI, and CCT of pc-wLEDs were measured under a current of 20 mA using an AvaSphere-50-IRRAD spectrophotometer and the corresponding AvaSoft 8 software.

2.3 Computation

Density functional theory (DFT) calculations of the BCBSO unit cell were performed using the Vienna *ab initio* simulation package (VASP).[46] The structure was first optimized with the Perdew–Burke–Ernzerhof (PBE) exchange and correlation functional.[47] A cutoff energy of 500 eV was used, and the integration of the first Brillouin zone was carried out using a Gamma-centered grid of 4 × 4 × 4. A PBE indirect bandgap of 4.86 eV was obtained from the band structure and density of states (DOS) calculations. To correct the significant underestimation of the PBE bandgap, the HSE06 functional was also implemented using a 4 × 4 × 4 *k*-point grid and a cut-off energy of 500 eV.[48] The Debye temperature (Θ_D) of BCBSO was approximated based on eqn (1),[49,50]

$$\Theta_D = \frac{h}{k_B}\left[6\pi^2 V^{\frac{1}{2}} N\right]^{\frac{1}{3}} \sqrt{\frac{B}{M}} f(v) \quad (1)$$

where h is the Planck constant, k_B is the Boltzmann constant, V is the unit cell volume, N is the number of atoms in the unit cell, B is the bulk modulus of the host, M is the molecular mass of the unit cell, and $f(v)$ is

$$f(v) = \left\{3\left[2\left(\frac{2}{3}\frac{1+v}{1-2v}\right)^{\frac{3}{2}} + \left(\frac{1}{3}\frac{1+v}{1-v}\right)^{\frac{3}{2}}\right]^{-1}\right\}^{\frac{1}{3}} \quad (2)$$

where v is the Poisson's ratio. B and v were derived using Voigt–Reuss–Hill (VRH) approximations based on the elastic tensor determined with VASP.[46,51]

3. Results and discussion

3.1 Structure and morphology

The phase purity of the as-prepared BCBSO:xCe^{3+} (x = 0–0.05) was first checked using laboratory powder X-ray diffraction, shown in Fig. 1a. All of the diffraction peaks were accounted for according to the published $Ba_2CaB_2Si_4O_{14}$ crystal structure (ICSD card no. 193536).[39] These products were further analyzed using synchrotron X-ray powder diffraction. Rietveld refinements of these data provide reliable crystal structure information. As shown in Fig. 1b, the diffractograms of the pristine, unsubstituted sample can be easily refined *via* the resulting refinement statistics and refined crystal structure data listed in Table 1 and Table S1 (ESI†). BCBSO crystallizes in a large tetragonal unit cell with space group $I\bar{4}2m$ (no. 121), as illustrated in Fig. 1c. It is composed of corner-sharing [SiO_4] and [BO_4] tetrahedra that create channels along each axis, which accommodate the Ba^{2+} and Ca^{2+} ions. The Ba^{2+} ion is located at the Wyckoff position 8i and is coordinated to 9 oxygen atoms, forming a distorted elongated square pyramid. The [BaO_9] unit has a volume of 41.102(5) Å^3 and an average Ba–O bond length of 2.889(4) Å. The Ca^{2+} ion is located at the Wyckoff position 4e and is coordinated to 6 oxygen atoms. The [CaO_6] triangular prism has a much smaller polyhedral volume of 13.073(7) Å^3 and an average Ca–O bond length of 2.377(1) Å. The ionic radius of Ba^{2+} is 1.47 Å (CN = 9) and of Ca^{2+} is 1 Å (CN = 6), which makes both ions suitable for Ce^{3+} substitution ($r_{CN=9}$ = 1.196 Å and $r_{CN=6}$ = 1.01 Å).[52] Thus, it is possible for dual-site substitution to produce two distinct luminescent centers, Ce_{Ba}^{3+} and Ce_{Ca}^{3+}.

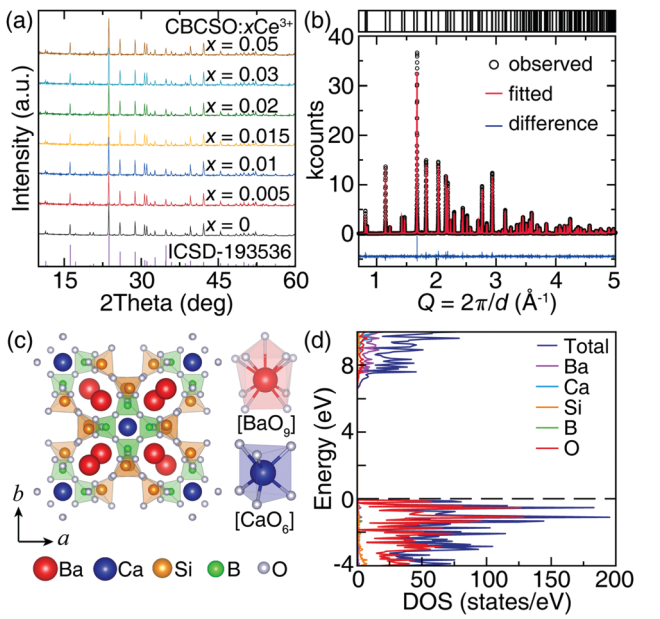

Fig. 1 (a) Powder X-ray diffractograms of $(Ba_2Ca)_{1-2x/3}Ce_xLi_xB_2Si_4O_{14}$ (BCBSO:xCe^{3+}, x = 0–0.05) with a reference pattern from ICSD card no. 193536, (b) rietveld refinement of BCBSO using a high-resolution synchrotron powder X-ray diffractogram, (c) crystal structure of BCBSO host and the [BaO_9] polyhedron and [CaO_6] trigonal prism, (d) projected total density of states (DOS) of BCBSO calculated with the hybrid DFT method.

Table 1 Rietveld refinement data of $Ba_2CaB_2Si_4O_{14}$

Formula	$Ba_2CaB_2Si_4O_{14}$
Radiation type; λ (Å)	Synchrotron; 0.457893
2θ range (deg)	1–50
Temperature (K)	295
Crystal system	Tetragonal
Space group (no.)	$I\bar{4}2m$ (121)
Z	4
a (Å)	10.93863(1)
c (Å)	10.28487(1)
V (Å^3)	1230.62(2)
R_p	0.0650
R_{wp}	0.0814
χ^2	2.436

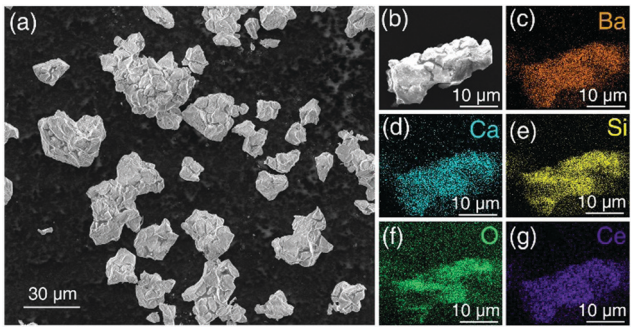

Fig. 2 (a) SEM micrographs of the BCBSO:0.03Ce^{3+} phosphor particles, (b) an enlarged view of a selected particle, and (c–g) EDS elemental mappings of the selected particle for Ba, Ca, Si, O, and Ce, respectively.

The band structure and density of states (DOS) of the BCBSO host calculated using DFT-PBE are illustrated in Fig. S1 (ESI†). An indirect bandgap (E_g) of 4.86 eV is obtained. This value is likely underestimated by ~40% owing to the inherent shortcomings of the PBE exchange and correlation functional. The electronic structure was further analyzed using the hybrid DFT functional HSE06 to calculate the electronic structure of BCBSO. As shown in Fig. 1d, the resulting DOS has a larger bandgap of 6.5 eV, which is likely much closer to the real value. This wide bandgap is advantageous for BCBSO as a phosphor host, especially when considering the possibility of photoionization induced thermal quenching.[50,53] Research has also shown that the quantum efficiency of a phosphor is related to the structural rigidity of the host, which can be described with Θ_D. Phosphors with a higher Θ_D tend to exhibit higher-energy phonon modes that decrease the probability of non-radiative relaxation and thus increase quantum efficiency.[50,54] Here, the Θ_D of the BCBSO compound was calculated to be 495 K using the *ab initio* method within the quasi-harmonic Debye model. This value is comparable to that of commercial blue phosphor host $BaMgAl_{10}O_{17}$ (478 K),[55] indicating that the BCBSO phosphor can probably achieve a high quantum efficiency. The combination of the wide bandgap and the high Θ_D of BCBSO makes it a promising inorganic host for preparing an efficient, thermally robust phosphor.

Fig. 2a shows SEM images of BCBSO:0.03Ce^{3+}. The crystallites are all aggregated and irregular in shape. The particle size is estimated to be several tens of microns. The EDS elemental mappings (Fig. 2b–g) of a selected particle indicate that Ba, Ca, Si, O, and Ce are homogeneously dispersed within the phosphor particle. The elemental mapping of B is not presented here, because it is too light to be reliably detected.

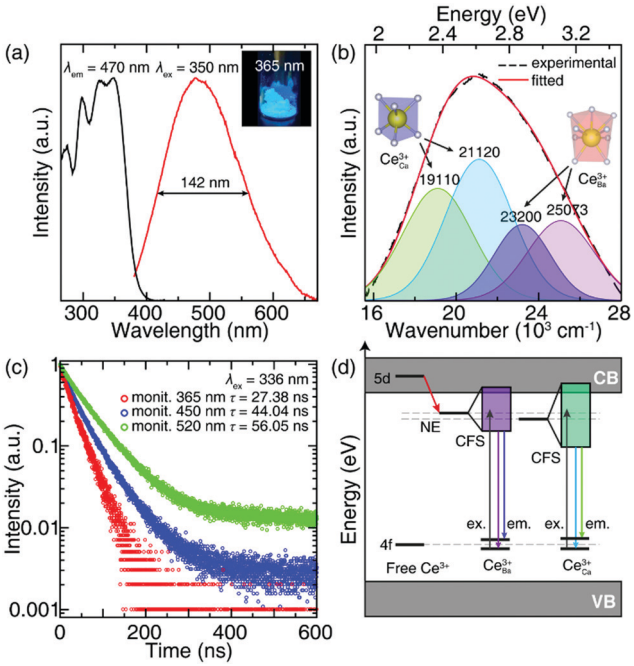

Fig. 3 (a) Photoluminescence excitation and emission spectra of BCBSO:0.03Ce^{3+} phosphor at room temperature; the inset shows a photograph of the phosphor under an ultraviolet lamp (λ_{ex} = 365 nm), (b) Gaussian fitting for the emission band of BCBSO:0.03Ce^{3+} under the excitation of 340 nm, (c) room temperature photoluminescence lifetime decay curves of BCBSO:0.03Ce^{3+} monitored at 365, 450 and 520 nm, respectively, using a 336 nm nano-LED as the excitation source, (d) energy level schematic diagram of BCBSO:Ce^{3+}. NE, CFS, CB, and VB represent the nephelauxetic effect, crystal field splitting, conduction band, and valence band, respectively.

3.2 Photoluminescence

The synthesis of the phase-pure BCBSO:xCe^{3+} allows for reliable analysis of its photoluminescence properties. Fig. 3a presents the emission and excitation spectra of BCBSO:0.03Ce^{3+} measured at room temperature. The inset of the figure shows that the sample exhibits a uniform cyan color under 365 nm excitation. This phosphor has a broadband excitation spectrum (λ_{em} = 470 nm) ranging from 250 to 400 nm, which stems from the electronic transitions from the Ce^{3+} 4f ground state to five various 5d excited states.[56] Under 350 nm excitation, it displays an intense and broadband cyan emission, corresponding to the ensuing spin–orbit coupled 5d → 4f ($^2F_{7/2}$ and $^2F_{5/2}$) relaxation. The maximum intensity of this process occurs at 478 nm with a fwhm of 142 nm (6053 cm^{-1}). The fwhm is further broadened to 161 nm (8010 cm^{-1}) under higher energy excitation (λ_{ex} = 340 nm), as shown in Fig. S2b and Table S2 (ESI†). This fwhm value is much larger than most of the reported cyan-emitting phosphors, making it a promising option to cover the blue,

cyan, and green regions of the visible spectrum simultaneously. The broad emission band (λ_{ex} = 340 nm) can be deconvoluted into four Gaussian sub-bands centered at 25 073 cm^{-1} (399 nm), 23 200 cm^{-1} (431 nm), 21 120 cm^{-1} (473 nm) and 19 110 cm^{-1} (523 nm), as presented in Fig. 3b, indicating the presence of two different Ce^{3+} luminescent centers. This is further substantiated by monitoring the excitation spectra at different emissions. According to the data in Fig. S2 (ESI†), the peaks in the excitation spectrum evolve in both shape and position, depending on the monitoring wavelength. Compared to the excitation spectrum monitored at 400 nm (a short wavelength), an additional excitation band appears at about 350 nm that gradually increases when monitored at a longer wavelength. This peak eventually becomes the most intense excitation band. Similarly, the emission spectrum changes as a function of excitation wavelength. These results confirm that Ce^{3+} ions occupy two different crystallographic sites, forming two distinct luminescent centers. Based on the respective size of the [BaO_9] and [CaO_6] polyhedra, as discussed above, both the Ba^{2+} and Ca^{2+} ions can be substituted by Ce^{3+}. Following the crystal field theory, one can see that the crystal field strength of the local polyhedron determines the splitting width of the Ce^{3+} 5d excitation levels, which finally influences the emission of Ce^{3+}.[57] The crystal field strength around Ce^{3+} can be approximated by using eqn (3),[58]

$$D_q = \frac{ze^2r^4}{6R^5} \quad (3)$$

where D_q is the measurement of crystal field strength, z is the valence of the anion, e is the electron charge, r is the radius of the wave function, and R is the distance between the central ion and its ligands. According to the refined crystal structure, the average bond length of Ba–O (2.889(4) Å) is much longer than that of Ca–O (2.377(1) Å), therefore the Ce^{3+} ion residing at the Ca^{2+} site will have a shorter distance from O^{2-} ions than that at the Ba^{2+} site. As shown in eqn (3), a shorter bond length between the central ion and its ligands will result in stronger crystal field splitting; thus, Ce^{3+} will produce a lower energy emission (longer emission wavelength).[57,59] Furthermore, a shorter Ce–O bond will also lead to a larger nephelauxetic effect, which pushes the Ce^{3+} 5d level down toward the 4f level. This also causes a longer emission wavelength.[32,59] Therefore, we can conclude that the higher energy emission bands (shorter emission wavelength) are attributed to Ce^{3+} occupying the Ba^{2+} site (Ce_{Ba}^{3+}), whereas the lower energy emission bands (longer emission wavelength) originate from Ce^{3+} substituting for Ca^{2+} (Ce_{Ca}^{3+}).

The time-resolved photoluminescence spectra provide additional evidence for the site occupancy. Fig. 3c shows the decay curves of BCBSO:0.03Ce^{3+} monitored at different emission wavelengths under the excitation of 336 nm. The decay curve monitored at 450 nm can be fitted using a bi-exponential function in eqn (4),[60]

$$I = A_1 \exp\left(-\frac{t}{\tau_1}\right) + A_2 \exp\left(-\frac{t}{\tau_2}\right) \quad (4)$$

where I is the luminescence intensity at time t, τ_1 and τ_2 are the fast and slow components of the lifetime, and A_1 and A_2 are the corresponding fitting parameters. The values of τ_1 and τ_2 and their percentage contents are provided in Table S3 (ESI†). The bi-exponential decay curve indicates that the emission arises from Ce^{3+} occupying two different lattice sites, which is consistent with the steady-state photoluminescence analysis. Moreover, monitoring the decay curves at 365 and 520 nm, as shown in Fig. 3c, one can observe a single exponential function with lifetimes of 27.38 and 56.05 ns, respectively. These luminescence lifetimes correspond to the emissions from the Ce_{Ba}^{3+} and Ce_{Ca}^{3+} centers, respectively. According to the values of τ_1 and τ_2, the average lifetime monitored at 450 nm was calculated to be 44.04 ns, which is typical for Ce^{3+}-substituted phosphors.[31,57] Additional decay curves for the samples with different Ce^{3+} concentrations are given in Fig. S3 (ESI†), and they all display the same behavior.

Based on all the information obtained from optical spectroscopy, it is possible to schematically illustrate the relative energy levels of Ce^{3+} ions in the BCBSO host. Fig. 3d shows that each of Ce^{3+} ions occupying different crystallographic sites experiences a different nephelauxetic effect and crystal field splitting resulting in different photoluminescence properties. These two distinct luminescent centers combine to produce the broadband cyan emission of BCBSO:Ce^{3+}.

Analyzing the normalized emission spectra of BCBSO:$x$$Ce^{3+}$ with different dopant concentrations (x = 0.005–0.05) under an excitation of 340 nm at room temperature, as plotted in Fig. 4a, provides additional information about this compound. There is a clear red shift and also a shape change in the emission spectra as the Ce^{3+} concentration is increased. This likely arises from different emission contributions of Ce_{Ba}^{3+} and Ce_{Ca}^{3+} in the total profile. Factors such as site occupancy, reabsorption, and emission band broadening may cooperatively influence the position and shape of the total emission spectra.[17] Tracking each emission spectrum, we can see that the shorter wavelength contribution of Ce_{Ba}^{3+} is much larger at a low concentration (*i.e.*, x = 0.005) compared to a higher one (*i.e.*, x = 0.05). This is because the $Ce_{Ba}^{3+}/Ce_{Ca}^{3+}$ ratio decreases with the increasing dopant concentration. The origin of this site preference is due to the fact that Ce^{3+} is smaller than Ba^{2+}

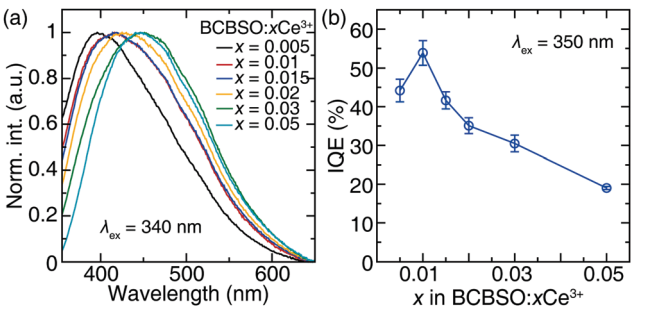

Fig. 4 (a) Normalized emission spectra under 340 nm excitation and (b) internal quantum efficiency (IQE) under 350 nm excitation of BCBSO:$x$$Ce^{3+}$ phosphors (x = 0.005–0.05).

but slightly larger than Ca^{2+}. As a result, Ce^{3+} firstly occupies the Ba^{2+} site at low concentrations before entering the smaller Ca^{2+} site. A similar site occupancy preference has been observed in other hosts with multiple substitution sites, and also results in similar evolutions of the emission spectra as the dopant concentration is changed.[17,34,61,62] Reabsorption can also be a possible reason for the evolution of the photoluminescence spectra with increasing x. It can be seen that the 350–400 nm emission originating from Ce_{Ba}^{3+} overlaps the lowest energy excitation band of Ce_{Ca}^{3+}. Thus, the Ce_{Ba}^{3+} emission can be reabsorbed, leading to a decrease in the emission intensity.[32] However, reabsorption is minimized at low substitution concentrations.

To evaluate the luminescence efficiency of BCBSO:xCe^{3+}, the IQE at various concentrations was measured. As shown in Fig. 4b, the sample containing 1% Ce^{3+} has the highest IQE of about 54% (λ_{ex} = 350 nm) at room temperature. Increasing the Ce^{3+} concentration causes a drop in IQE, which is a common phenomenon, the so-called concentration quenching, in phosphor materials, likely stemming from energy transfer between adjacent luminescent centers, such as exchange interactions, radiation reabsorption, or multipole–multipole interactions.[31,53] The IQE value is still reasonable and can be improved by optimizing the synthesis conditions as well as post-processing the particle morphology of the phosphor.

3.3 Thermal quenching

Phosphors in pc-wLEDs experience moderately high temperatures during operation.[4,63] Thus, it is important to evaluate the thermal and chromaticity stabilities of the BCBSO:Ce^{3+} phosphor as a function of temperature. The temperature-dependent emission spectra of BCBSO:0.03Ce^{3+} were collected from 300 to 580 K (λ_{ex} = 340 nm). The resulting contour plot, normalized integrated emission intensity and the normalized peak intensity against temperature are plotted in Fig. 5. The raw spectra are provided in Fig. S4 (ESI†). A slight blue shift of the emission spectra with increasing temperature is observed (Fig. 5a), which stems from the lattice expansion of the BCBSO host with increasing temperature. Fortunately, this change causes only a minimal shift in the chromaticity coordinates (Fig. S4c, ESI†), indicating the superb color stability. More importantly, plotting the normalized integrated emission intensity and normalized peak intensity as a function of temperature (Fig. 5b) reveals BCBSO:0.03Ce^{3+} maintains 95% of the room temperature luminescence at 420 K. Further increasing the temperature to 580 K indicates that the phosphor still maintains 80% of the emission intensity. This excellent thermal stability can be attributed to the large band gap (E_g = 6.5 eV) and relatively rigid crystal structure (Θ_D = 495 K) of the BCBSO host. Such a thermally robust cyan-emission provides great promise for applications even in high-power pc-wLEDs.

3.4 Application in pc-wLEDs

The broadband cyan emission and excellent thermal stability make BCBSO:Ce^{3+} a promising component for high-quality, full-visible-spectrum white LED lighting. Therefore, a simple

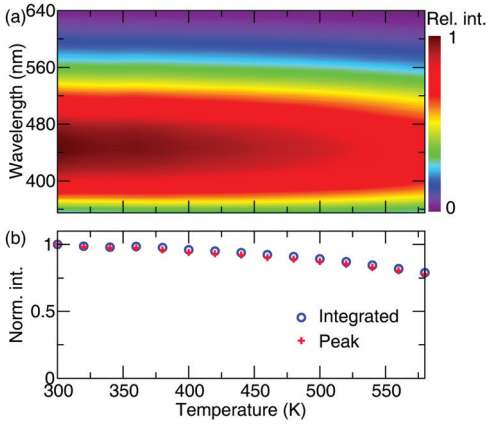

Fig. 5 (a) Contour plot of the temperature-dependent emission spectra of the BCBSO:0.03Ce^{3+} phosphor under 340 nm excitation, and (b) the normalized integrated emission intensity and peak intensity as a function of temperature.

dichromatic white LED device (wLED-1) was fabricated by coupling the as-prepared cyan-emitting BCBSO:0.03Ce^{3+} phosphor and a red-emitting $Sr_2Si_5N_8$:Eu^{2+} to a UV LED (λ_{ex} = 370 nm). The device was driven by a current of 20 mA to yield the corresponding luminescence spectrum (Fig. 6a upper). Because of the broad cyan emission from BCBSO:Ce^{3+} and broad red emission from $Sr_2Si_5N_8$:Eu^{2+}, a continuous spectrum covering the entire visible region was achieved even without mixing an additional green-emitting phosphor usually used in other full-visible-spectrum pc-wLEDs. The wLED-1 device produces the high-quality cool white light with the CIE 1931 chromaticity coordinates of (0.305, 0.321), a CCT of 7052 K, and a R_a of 91, as plotted in Fig. 6b. The color rendering indexes ($R_1 \sim R_{15}$) listed in Table S4 (ESI†) indicate that it also has very high R_9 (96) and R_{12} (85) values. The high color rendering cool white light has great potential in special applications, for example, medical lighting. To further tune the CCT of the pc-wLED, a green-emitting β-SiAlON:Eu^{2+} phosphor was added to the mixture of BCBSO:0.03Ce^{3+} and $Sr_2Si_5N_8$:Eu^{2+}. The addition of green can finely tune the CCT of the white light along the

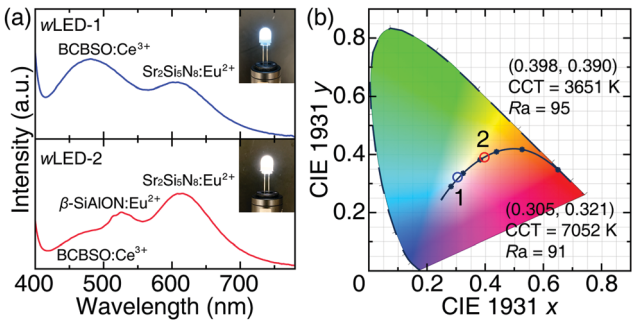

Fig. 6 (a) Luminescence spectra of two pc-wLEDs: wLED-1 fabricated by combining the cyan-emitting BCBSO:0.03Ce^{3+}, red-emitting $Sr_2Si_5N_8$:Eu^{2+}, and a 370 nm UV-LED; wLED-2 fabricated by adding an additional β-SiAlON:Eu^{2+} green-emitting phosphor. The insets show the corresponding pc-wLED devices driven by a current of 20 mA. (b) The CIE 1931 chromaticity coordinates of the fabricated pc-wLEDs.

blackbody locus without sacrificing the R_a, resulting in high-quality cool to warm white lights. The fabricated wLED-2 (Fig. 6a lower and Fig. 6b) produces a warm white light with the chromaticity coordinates of (0.398, 0.390), a CCT of 3651 K, and an improved R_a of 95. These results validate the outstanding potential of the newly developed BCBSO:Ce^{3+} cyan-emitting phosphor in future UV-driven pc-wLEDs.

4. Conclusions

In summary, we have developed a novel cyan-emitting borosilicate phosphor, $Ba_2CaB_2Si_4O_{14}$:Ce^{3+}, for use in full-visible-spectrum pc-wLEDs. The phosphor exhibits a broadband cyan emission (fwhm = 142 nm; 6053 cm^{-1}) peaking at 478 nm, simultaneously covering the blue, cyan and green light regions in the visible spectrum. The broadband emission stems from the dual-site occupancy of Ce^{3+} on both Ba^{2+} and Ca^{2+} crystallographic sites in the crystal structure. This is proven using the crystal structure and photoluminescence analysis. The phosphor shows a relatively high IQE of 54% and excellent thermal stability with 95% emission intensity retention at 420 K. Combining the broadband cyan-emitting BCBSO:Ce^{3+} with a single red-emitting phosphor allows the production of a UV-driven high quality (R_a = 91) cool white light (CCT = 7052 K). The CCT can be finely tuned in a wide range from the cool to the warm by introducing an additional green-emitting phosphor. This work not only provides a promising cyan-emitting phosphor for high-quality full-visible-spectrum pc-wLEDs, but also demonstrates an excellent example of multi-site engineering in phosphor design.

Conflicts of interest

There are no conflicts to declare.

Acknowledgements

The authors are grateful for the financial supports from the National Natural Science Foundation of China (no. 51832005 and 51572232), the National Key Research and Development Program of China (MOST, 2017YFB0404301), the National Science Foundation (DMR 18-47701 and CER 19-11311), and the Welch Foundation (E-1981). S. Y. also thanks the financial support from the China Scholarship Council during his study in Houston.

References

1 E. F. Schubert and J. K. Kim, *Science*, 2005, **308**, 1274–1278.
2 P. Pust, P. J. Schmidt and W. Schnick, *Nat. Mater.*, 2015, **14**, 454–458.
3 G. J. Hoerder, M. Seibald, D. Baumann, T. Schröder, S. Peschke, P. C. Schmid, T. Tyborski, P. Pust, I. Stoll, M. Bergler, C. Patzig, S. Reißaus, M. Krause, L. Berthold, T. Höche, D. Johrendt and H. Huppertz, *Nat. Commun.*, 2019, **10**, 1824.
4 L. Wang, R.-J. Xie, T. Suehiro, T. Takeda and N. Hirosaki, *Chem. Rev.*, 2018, **118**, 1951–2009.
5 P. Pust, V. Weiler, C. Hecht, A. Tücks, A. S. Wochnik, A.-K. Henß, D. Wiechert, C. Scheu, P. J. Schmidt and W. Schnick, *Nat. Mater.*, 2014, **13**, 891–896.
6 Y. H. Kim, P. Arunkumar, B. Y. Kim, S. Unithrattil, E. Kim, S.-H. Moon, J. Y. Hyun, K. H. Kim, D. Lee, J.-S. Lee and W. B. Im, *Nat. Mater.*, 2017, **16**, 543–550.
7 I. Jaadane, P. Boulenguez, S. Chahory, S. Carré, M. Savoldelli, L. Jonet, F. Behar-Cohen, C. Martinsons and A. Torriglia, *Free Radical Biol. Med.*, 2015, **84**, 373–384.
8 S. M. Pauley, *Med. Hypotheses*, 2004, **63**, 588–596.
9 J. H. Oh, S. J. Yang and Y. R. Do, *Light: Sci. Appl.*, 2014, **3**, e141.
10 J. K. Sheu, S. J. Chang, C. H. Kuo, Y. K. Su, L. W. Wu, Y. C. Lin, W. C. Lai, J. M. Tsai, G. C. Chi and R. K. Wu, *IEEE Photonics Technol. Lett.*, 2003, **15**, 18–20.
11 T. Nishida, T. Ban and N. Kobayashi, *Appl. Phys. Lett.*, 2003, **82**, 3817–3819.
12 J. McKittrick, M. E. Hannah, A. Piquette, J. K. Han, J. I. Choi, M. Anc, M. Galvez, H. Lugauer, J. B. Talbot and K. C. Mishra, *ECS J. Solid State Sci. Technol.*, 2013, **2**, R3119–R3131.
13 M. Zhao, H. Liao, M. S. Molokeev, Y. Zhou, Q. Zhang, Q. Liu and Z. Xia, *Light: Sci. Appl.*, 2014, **8**, 38.
14 M.-H. Fang, C. Ni, X. Zhang, Y.-T. Tsai, S. Mahlik, A. Lazarowska, M. Grinberg, H.-S. Sheu, J.-F. Lee, B.-M. Cheng and R.-S. Liu, *ACS Appl. Mater. Interfaces*, 2016, **8**, 30677–30682.
15 C. Yan, Z. Liu, W. Zhuang, R. Liu, X. Xing, Y. Liu, G. Chen, Y. Li and X. Ma, *Inorg. Chem.*, 2017, **56**, 11087–11095.
16 Y. Liu, J. Silver, R.-J. Xie, J. Zhang, H. Xu, H. Shao, J. Jiang and H. Jiang, *J. Mater. Chem. C*, 2017, **5**, 12365–12377.
17 W. Zhou, F. Pan, L. Zhou, D. Hou, Y. Huang, Y. Tao and H. Liang, *Inorg. Chem.*, 2016, **55**, 10415–10424.
18 J. Zhong, J. Li, M. Liu, K. Wang, Y. Zhu, X. Li, Z. Ji and D. Chen, *J. Am. Ceram. Soc.*, 2019, **102**, 7376–7385.
19 Y. Zhou, W. Zhuang, Y. Hu, R. Liu, H. Xu, M. Chen, Y. Liu, Y. Li, Y. Zheng and G. Chen, *Inorg. Chem.*, 2019, **58**, 1492–1500.
20 X. Wang, Z. Zhao, Q. Wu, Y. Li and Y. Wang, *J. Mater. Chem. C*, 2016, **4**, 11396–11403.
21 L. Sun, B. Devakumar, J. Liang, S. Wang, Q. Sun and X. Huang, *J. Mater. Chem. C*, 2020, **8**, 1095–1103.
22 J. Liang, B. Devakumar, L. Sun, S. Wang, Q. Sun and X. Huang, *J. Mater. Chem. C*, 2020, **8**, 4934–4943.
23 H.-L. Li, R.-J. Xie, G.-H. Zhou, N. Hirosaki and Z. Sun, *J. Electrochem. Soc.*, 2010, **157**, J251–J255.
24 Q. Wu, Z. Yang, Z. Zhao, M. Que, X. Wang and Y. Wang, *J. Mater. Chem. C*, 2014, **2**, 4967–4973.
25 P. Strobel, T. de Boer, V. Weiler, P. J. Schmidt, A. Moewes and W. Schnick, *Chem. Mater.*, 2018, **30**, 3122–3130.
26 S.-P. Lee, C.-H. Huang, T.-S. Chan and T.-M. Chen, *ACS Appl. Mater. Interfaces*, 2014, **6**, 7260–7267.
27 W. Zhou, J. Han, X. Zhang, Z. Qiu, Q. Xie, H. Liang, S. Lian and J. Wang, *Opt. Mater.*, 2015, **39**, 173–177.
28 P. Dang, D. Liu, Y. Wei, G. Li, G. H. Lian, M. Shang and J. Lin, *Inorg. Chem.*, 2020, **59**, 6026–6038.

29 B. Li, J. Liang, L. Sun, S. Wang, Q. Sun, B. Devakumar, G. Annadurai, D. Chen, X. Huang and Y. Wu, *J. Lumin.*, 2019, **211**, 388–393.
30 X. Huang, H. Guo, L. Sun, T. Sakthivel and Y. Wu, *J. Alloys Compd.*, 2019, **787**, 865–871.
31 J. Zhong, Y. Zhuo, S. Hariyani, W. Zhao, J. Wen and J. Brgoch, *Chem. Mater.*, 2020, **32**, 882–888.
32 Q.-Q. Zhu, L. Wang, N. Hirosaki, L. Y. Hao, X. Xu and R.-J. Xie, *Chem. Mater.*, 2016, **28**, 4829–4839.
33 L. Wang, J. Cui, Q. Shi, Y. Tian, C. Cui, M. Ren and P. Huang, *J. Alloys Compd.*, 2018, **764**, 1003–1007.
34 Q. Wei, J. Ding and Y. Wang, *Chem. Eng. J.*, 2020, **386**, 124004.
35 V. Rajendran, M.-H. Fang, G. N. D. Guzman, T. Lesniewski, S. Mahlik, M. Grinberg, G. Leniec, S. M. Kaczmarek, Y.-S. Lin, K.-M. Lu, C.-M. Lin, H. Chang, S.-F. Hu and R.-S. Liu, *ACS Energy Lett.*, 2018, **3**, 2679–2684.
36 V. Rajendran, T. Lesniewski, S. Mahlik, M. Grinberg, G. Leniec, S. M. Kaczmarek, W.-K. Pang, Y.-S. Lin, K.-M. Lu, C.-M. Lin, H. Chang, S.-F. Hu and R.-S. Liu, *ACS Photonics*, 2019, **6**, 3215–3224.
37 D. Sun, L. Zhang, Z. Hao, X. Zhang, G.-H. Pan, H. Wu, Y. Luo, S. He, H. Zhao and J. Zhang, *Dalton Trans.*, 2018, **47**, 16723–16728.
38 H. Zeng, T. Zhou, L. Wang and R.-J. Xie, *Chem. Mater.*, 2019, **31**, 5245–5253.
39 A. R. Kampf, R. C. Peterson and B. R. Joy, *Can. Mineral.*, 2014, **52**, 401–407.
40 P. L. Lee, D. Shu, M. Ramanathan, C. Preissner, J. Wang, M. A. Beno, R. B. Von Dreele, L. Ribaud, C. Kurtz, S. M. Antao, X. Jiao and B. H. Toby, *J. Synchrotron Radiat.*, 2008, **15**, 427–432.
41 B. H. Toby, *J. Appl. Crystallogr.*, 2001, **34**, 210–213.
42 A. C. Larson and R. B. Von Dreele, General Structure Analysis System (GSAS), Los Alamos National Laboratory Report LAUR 86-748, Los Alamos, New Mexcico, 2004.
43 K. Momma and F. Izumi, *J. Appl. Crystallogr.*, 2011, **44**, 1272–1276.
44 S. Leyre, E. Coutino-Gonzalez, J. J. Joos, J. Ryckaert, Y. Meuret, D. Poelman, P. F. Smet, G. Durinck, J. Hofkens, G. Deconinck and P. Hanselaer, *Rev. Sci. Instrum.*, 2014, **85**, 123115.
45 J. C. de Mello, H. F. Wittmann and R. H. Friend, *Adv. Mater.*, 1997, **9**, 230–232.
46 G. Kresse and J. Furthmüller, *Phys. Rev. B: Condens. Matter Mater. Phys.*, 1996, **54**, 11169–11186.
47 P. E. Blöchl, *Phys. Rev. B: Condens. Matter Mater. Phys.*, 1994, **50**, 17953–17979.
48 J. Heyd, G. E. Scuseria and M. Ernzerhof, *J. Chem. Phys.*, 2003, **118**, 8207–8215.
49 E. Francisco, J. M. Recio, M. A. Blanco, A. M. Pendás and A. Costales, *J. Phys. Chem. A*, 1998, **102**, 1595–1601.
50 J. Brgoch, S. P. DenBaars and R. Seshadri, *J. Phys. Chem. C*, 2013, **117**, 17955–17959.
51 R. Hill, *Proc. Phys. Soc., Sect. A*, 1952, **65**, 349–354.
52 R. D. Shannon, *Acta Crystallogr., Sect. A: Cryst. Phys., Diffr., Theor. Gen. Crystallogr.*, 1976, **32**, 751–767.
53 Y. Zhuo, A. M. Tehrani, A. O. Oliynyk, A. C. Duke and J. Brgoch, *Nat. Commun.*, 2018, **9**, 4377.
54 K. A. Denault, J. Brgoch, S. D. Kloß, M. W. Gaultois, J. Siewenie, K. Page and R. Seshadri, *ACS Appl. Mater. Interfaces*, 2015, **7**, 7264–7272.
55 S. Hariyani, A. C. Duke, T. Krauskopf, W. G. Zeier and J. Brgoch, *Appl. Phys. Lett.*, 2020, **116**, 051901.
56 S. You, S. Li, P. Zheng, T. Zhou, L. Wang, L. Liu, N. Horisaki, F. Xu and R.-J. Xie, *Laser Photonics Rev.*, 2019, **13**, 1800216.
57 G. Blasse and B. C. Grabmaier, *Luminescent Materials*, Springer Verlag, Berlin, 1994.
58 M. Gerloch and R. C. Slade, *Ligand-field Parameters*, Cambridge University Press, London, 1973.
59 P. Dorenbos, *Phys. Rev. B: Condens. Matter Mater. Phys.*, 2001, **64**, 125117.
60 J. Qiao, L. Ning, M. S. Molokeev, Y.-C. Chuang, Q. Liu and Z. Xia, *J. Am. Chem. Soc.*, 2018, **140**, 9730–9736.
61 W. Zhou, Y. Ou, X. Li, M. G. Brik, A. M. Srivastava, Y. Tao and H. Liang, *Inorg. Chem.*, 2018, **57**, 14872–14881.
62 W. Ma, J. Zhang, X. Zhang, X. Zhang, S. Liao, Z. Qiu, W. Zhou, L. Yu and S. Lian, *J. Alloys Compd.*, 2018, **764**, 574–581.
63 M. Zhao, H. Liao, L. Ning, Q. Zhang, Q. Liu and Z. Xia, *Adv. Mater.*, 2018, **30**, 1802489.